

See discussions, stats, and author profiles for this publication at: <https://www.researchgate.net/publication/262951127>

Electron Transfer at Oxide/Water Interfaces Induced by Ionizing Radiation

ARTICLE in THE JOURNAL OF PHYSICAL CHEMISTRY C · MARCH 2014

Impact Factor: 4.77 · DOI: 10.1021/jp501396a

CITATIONS

3

READS

37

7 AUTHORS, INCLUDING:



D. Simeone

Atomic Energy and Alternative Energies Com...

97 PUBLICATIONS 692 CITATIONS

SEE PROFILE



Uli Schmidhammer

Université Paris-Sud 11

54 PUBLICATIONS 517 CITATIONS

SEE PROFILE



Mehran Mostafavi

Université Paris-Sud 11

162 PUBLICATIONS 2,917 CITATIONS

SEE PROFILE



Sophie Le Caer

Atomic Energy and Alternative Energies Com...

42 PUBLICATIONS 538 CITATIONS

SEE PROFILE

Electron Transfer at Oxide/Water Interfaces Induced by Ionizing Radiation

E. Chelnokov,[†] V. Cuba,[‡] D. Simeone,[§] J.-M. Guigner,^{||} U. Schmidhammer,[⊥] M. Mostafavi,[⊥] and S. Le Caër^{*,†}

[†]Institut Rayonnement Matière de Saclay Service Interdisciplinaire sur les Systèmes Moléculaires et les Matériaux, UMR 3299 CNRS/CEA SIS2M Laboratoire de Radiolyse, Bâtiment 546, F-91191 Gif-sur-Yvette Cedex, France

[‡]Faculty of Nuclear Sciences and Physical Engineering, Czech Technical University in Prague, Brehova 7, Prague 1, Czech Republic

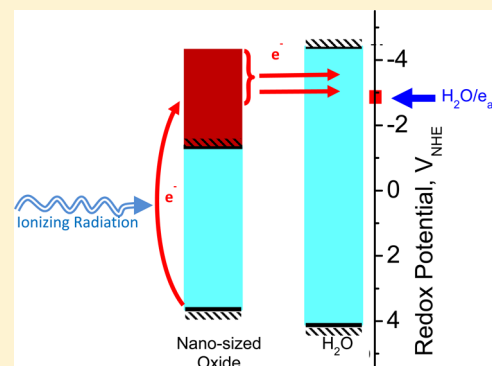
[§]Matériaux Fonctionnels pour l'Energie Equipe mixte CEA-CNRS-ECP DEN/DANS/DMN/SRMA/LA2M, CEA Saclay, F-91191 Gif sur Yvette, France

^{||}Institut de Minéralogie et de Physique des Milieux Condensés IMPMC, UMR 7590 CNRS, Université Pierre et Marie Curie, Tour 23, Campus de Jussieu, 4 Place Jussieu, F-75252 Paris Cedex 05, France

[⊥]Laboratoire de Chimie Physique, UMR 8000 CNRS/Université Paris-Sud 11, Bâtiment 349, F-91405 Orsay Cedex, France

S Supporting Information

ABSTRACT: The electron transfer from oxide into water is studied in nanoparticle suspensions of various oxides (SiO_2 , ZnO , Al_2O_3 , Nd_2O_3 , Sm_2O_3 , and Er_2O_3) by means of pulse and γ radiolysis. The time-resolved and steady-state investigations of the present study demonstrate independently that whatever the band gap and the electron affinity of the oxide, the electron transfer always takes place in these nanometric systems: Irradiation generates hot electrons which have enough energy to cross the semiconductor–liquid interface. Moreover, picosecond measurements evidence that the spectrum of the solvated electron is the same as in water. Lastly, the decay of the solvated electron is similar on the picosecond to nanosecond time scale in water and in these suspensions, but it is clearly different on the nanosecond to microsecond time scale.



Electron transfer across nanoparticle surfaces is a fundamental process which is relevant in many applications such as electrochemistry,^{1–3} catalysis,^{1,4–6} energy storage,^{7–9} molecular electronics,^{4,10–12} solar cells,^{3,13–17} etc.

Among different experimental techniques, radiolysis is an efficient tool to produce the electron and study its reactivity.^{18–26} γ and pulse radiolysis are then two appropriate tools of investigation. The former allows indirect electron detection by electron capture, and the latter direct electron concentration measurement by time-resolved absorption experiments. However, and despite its fundamental and practical interest,²⁷ phenomena occurring at semiconductor/liquid interfaces have been scarcely studied by means of radiolysis,^{28,29} and the parameters which affect and control the electron transfer under ionizing radiation are still not well understood.

In radiation chemistry, the key investigations were mainly performed in silica: experiments were carried out by means of (sub)nanosecond pulse radiolysis both in silica nanoparticle suspensions²⁸ and in silica-based controlled pore glasses,²⁹ and simulations were performed in porous silica.³⁰ In all these studies, the nature of the material remained the same (silica) and the characteristic size of the system was varied. These experimental studies have proven that energy absorbed by solid

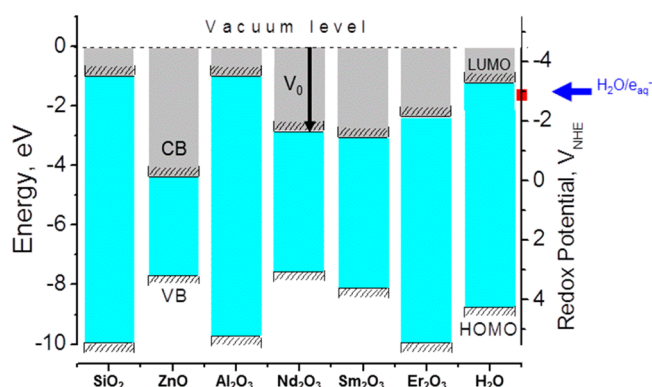
nanoparticles crosses the solid–liquid interface and generates hydrated electrons as a result of an interfacial charge transfer process.^{28,29} Moreover, Monte Carlo simulations have evidenced that the relative position of the conduction band edge V_0 (electron affinity) of water and silica plays a major role in the radiolysis of silica/water systems (see Scheme 1 for the definition of these terms).³⁰ In the cited work, the authors have attributed the enhancement of solvated electron yields in small pores to the fact that the conduction band edge V_0 is lower in water than in silica.³⁰

The aim of the present work is to extend the investigation of solid–liquid interfaces under ionizing radiation and particularly to measure the electron yields in various semiconductor/water systems. We have chosen to study suspensions of highly concentrated oxides (SiO_2 , ZnO , Al_2O_3 , Nd_2O_3 , Sm_2O_3 , and Er_2O_3) offering a large variety of band gaps and electron affinities (see Scheme 1 and Table 1). In these concentrated suspensions, a part of the radiation energy is absorbed by the particles. To make the comparison between the different

Received: February 8, 2014

Revised: March 24, 2014

Published: March 25, 2014

Scheme 1. Energy Levels for the Oxides under Study and for Water^a

^aFor the solids, the filled energy states correspond to the valence band (VB) and the empty states to the conduction band (CB; indicated in dark gray). The energy bands are separated by the band gap. The electron affinity (V_0) corresponds to the energy difference between the vacuum level and the bottom of the conduction band. The values (band gap, electron affinity) for the different oxides are given in Table 1. In solid-state physics, the vacuum level is taken as the zero-energy reference. For the sake of clarity, the band bending at the interface is not represented. In the case of water, the positions of the highest occupied molecular orbital (HOMO) and the lowest unoccupied molecular orbital (LUMO) are indicated with horizontal straight lines. The energy difference between the vacuum level and the LUMO is taken as -1.2 eV as reported in ref 30. Water is characterized by redox levels (for instance, the $\text{H}_2\text{O}/\text{e}_{\text{aq}}^-$ couple) which lie within the band gap of water. On the right scale, redox potentials vs NHE are given. The redox potential of the $\text{H}_2\text{O}/\text{e}_{\text{aq}}^-$ system is represented on this axis and is equal to -2.87 V.

Table 1. Purity, Band Gap, and Electron Affinity for the Oxides under Study

oxide	phase	purity (%)	band gap (eV)	electron affinity (V_0) (eV)
SiO_2	amorphous	99.5	9.0	-1.0
ZnO	hexagonal	99.99	3.3	-4.4
Al_2O_3	γ	99.97	8.8	-1
Nd_2O_3	cubic	99.9	4.7	-2.9
Sm_2O_3	cubic	99.9	5.1	-3.1
Er_2O_3	cubic	99.9	7.6	-2.4

systems relevant, the same particle size was chosen for all oxides (20 nm), as this distance (10–20 nm) was proven to be the escape depth of electrons in insulators.^{31,32} Then, if electron transfer happens, such characteristic nanometric distances are adequate to observe it and to evidence the processes occurring at interfaces.

EXPERIMENTAL SECTION

Materials. The powders (see Table 1 for their characteristics) used herein were purchased from NanoAmor (Al_2O_3 , Nd_2O_3 , Sm_2O_3 , and Er_2O_3) and from Sigma-Aldrich (SiO_2). They were of the highest purity available (Table 1). The ZnO nanoparticles were prepared according to the procedure described in ref 33. Moreover, all chemicals were of the highest quality commercially available.

Initial analysis of all powders using XRD (X-ray diffraction), TEM (transmission electron microscopy), and BET (Brunauer–Emmett–Teller) methods was performed to confirm the size of the particles and the presence, if relevant, of one oxide

phase (Table 1). The powders were thermally treated for 60 min at 140°C to remove adsorbed water followed by 60 min at 500°C to remove any organic contaminants. It was then checked by XRD analysis that this thermal treatment did not significantly change the size of the particles. All suspensions were then prepared using these freshly thermally treated powders and ultrapure water from a Milli-Q Advantage purification system (having a conductivity of $18.2\text{ M}\Omega$ and very low total organic carbon ($\text{TOC} < 10\text{ ppb}$)). To evidence the influence of the oxide, high concentrations of oxides were prepared (until 30 wt %). No surfactant was added to the solutions to prevent any artifact in the radiation chemistry experiments. In this case, the oxide nanoparticles tend to aggregate. To homogenize the suspensions, a 130 W ultrasonic atomizer was used with an optimized regime of ultrasonication (10 min at 40% amplitude, which minimizes the size of these aggregates;^{34–36} see Figure SI-1 in the Supporting Information). The suspensions were then carefully characterized by dynamic light scattering (DLS; Figure SI-1) and cryo-TEM techniques (see, for example, Figure SI-2 in the Supporting Information). The distribution by size of particle aggregates (typically a few hundred nanometers; see Figures SI-1 and SI-2) was found to be stable in suspensions under stirring for a few days after preparation. It remained stable for the time required to perform the experiment (a few hours). We assume that the aggregation of the nanoparticles does not change the radiolytic yields of the solvated electron.

We worked at the highest possible concentration for all the 20 nm oxides in water, which we will call hereafter the “apparent concentration”, $0.6\text{ mol}\cdot\text{dm}^{-3}$, and also at a higher apparent concentration, $2.2\text{ mol}\cdot\text{dm}^{-3}$, for the oxides having the lowest molar mass. The corresponding oxide mass fractions are given in Table 2.

To allow the comparison with previous work,²⁸ we also worked with Ludox colloidal silica purchased from Sigma-Aldrich and used as received. The TM-50 sample with 22 nm particles was studied. The solution is 50% silica by weight and is basic (pH 9). The particles are negatively charged with Na^+ counterions. Ludox is optically transparent, which enables pulse radiolysis experiments to be easily performed.

In all radiolysis experiments, the dose received by the oxide suspensions is equal to the dose D received by water (and determined experimentally using the electron absorption in pulse radiolysis experiments or the Fricke dosimeter in γ irradiation experiments) multiplied by a factor F accounting for the difference in electronic density between water and oxide. This factor is calculated according to the following equation:³⁷

$$F = \frac{M_{\text{H}_2\text{O}} N_{\text{ox}}^e}{M_{\text{ox}} N_{\text{H}_2\text{O}}^e} P + 1 - P$$

with M_{ox} = molar mass of the oxide, N_{ox}^e = number of electrons in the oxide, P = oxide mass fraction (for example, 0.2 for 20 wt %), $M_{\text{H}_2\text{O}}$ = molar mass of water ($18\text{ g}\cdot\text{mol}^{-1}$), and $N_{\text{H}_2\text{O}}^e$ = number of electrons in water (10)

The measured absorbance A can be written as $A = \epsilon \rho F D G$, with ϵ the solvated electron extinction coefficient, l the optical path length inside the flow cell, ρ the mass density of the suspension (or solution), FD the dose received by the system, and G the solvated electron radiolytic yield at the studied time. The calculations of the F factor are given in Table 2, together with the mass density of all the suspensions under study.

The different radiolysis experiments are described below.

Table 2. Calculation of the Dose Received by the Samples under Study^a

oxide	M_{ox} (g/mol)	N_{ox}^e	P (oxide mass fraction)	$(M_{\text{H}_2\text{O}}N_{\text{ox}}^e/M_{\text{ox}}N_{\text{H}_2\text{O}}^e)P$	F	mass density ρ (g·cm ⁻³)	ρF (g·cm ⁻³)	real optical path in 1 mm cell (mm)
Ludox	60	30	0.5	0.45	0.95	1.4	1.33	1
SiO ₂	60	30	0.038	0.034	0.996	1.01	1.01	1
SiO ₂ (2.2 M)	60	30	0.125	0.112	0.987	1.06	1.05	1.5
ZnO	81	38	0.05	0.042	0.992	1.01	1.00	
ZnO (2.2 M)	81	38	0.157	0.132	0.972	1.15	1.12	3.0
Al ₂ O ₃	102	50	0.0625	0.055	0.99	1.05	1.04	1.1
Al ₂ O ₃ (2.2 M)	102	50	0.2	0.176	0.976	1.15	1.12	2.0
Nd ₂ O ₃	336	144	0.18	0.14	0.96	1.17	1.12	
Sm ₂ O ₃	348	148	0.185	0.142	0.957	1.17	1.12	5.8
Er ₂ O ₃	382	160	0.2	0.15	0.95	1.19	1.13	

^aThis dose is equal to the dose D received by water multiplied by a factor F^{37} accounting for the difference in electronic density between water and oxide whose calculation is presented in the text. N_{ox}^e is the number of electrons in the oxide. The molar mass of water is 18 g·mol⁻¹, and the number of electrons in water is equal to 10. Unless otherwise specified (in the case of the 2.2 mol·dm⁻³ apparent concentration), the apparent concentration of the oxide is 0.6 mol·dm⁻³. The mass density of each suspension is also given together with the real optical path determined using dyes in the suspensions in a 1 mm optical path cell.

Pulse Radiolysis. Because of the scattering of the solutions, a limited number of samples were studied by pulse radiolysis.

The ultrafast kinetics of the nanoparticle suspensions was accessed by picosecond pulse radiolysis with the laser-driven electron accelerator ELYSE.³⁸ A pump–probe setup installed at experimental area 1 was used whose basic optical configuration and data acquisition scheme are described in ref 26. The transient absorbance of the samples was probed in a flow cell with a 5 mm nominal optical path collinear to the electron pulse propagation; the electron pulses were delivered with a pulse duration of about 10 ps and an electron energy of 7.6 MeV at a repetition rate of 10 Hz. For the strongly diffusing nanoparticle samples, the fundamental laser wave of a chirped pulse amplification Ti:sapphire laser at 782 nm was used as a probe with a pulse duration of about 100 fs; the available energy was adjusted to adapt the probe light level transmitted by the sample to the dynamic range of the photodetector. In the case of the optically transparent Ludox sample, broad-band probing with a supercontinuum generated in CaF₂ was possible, allowing transient spectra to be recorded over the visible range. The dose per pulse was typically around 18 Gy.

To span the nanosecond to microsecond time range, we used the ALIENOR electron linear accelerator, which delivers 10 MeV electrons.³⁹ Electron pulses of 10 ns full width at half-maximum (fwhm) were used. The dose per pulse was determined by measuring the absorbance of the solvated electron and was found to be 100 Gy/pulse. The repetition rate of the electron pulses was 10 Hz. Transient absorption measurements of the nanoparticle suspensions were recorded at 633 nm using a 10 mW HeNe laser as the probe light. At this wavelength, the hydrated electron extinction coefficient is 15800 dm³·mol⁻¹·cm⁻¹.⁴⁰ The suspensions were flowed in a 1 mm optical path Suprasil cell. All measurements were performed after careful Ar bubbling. The signal due to the electron was then obtained after subtraction of the signal obtained after N₂O bubbling. The spectrum of the electron could also be obtained under the same conditions, using a 450 W Xe lamp as the probe light and an ICCD camera (PIMAX3, Princeton Instruments) providing an efficient signal accumulation to detect the solvated electron. Typically 1000 spectra were accumulated, and the spectra were recorded 40 ns after the electron pulse.

It is well-known that scattering can affect the optical path of the probe light.⁴¹ The real optical path was determined in each

suspension under study in 1 mm cells with the help of dyes as reference. For this purpose, two different dyes were used: patent blue V (positively charged dye) and bromophenol blue (anionic sulfonephthalein dye). To minimize the interactions between the nanoparticles and the dye, patent blue V was used in the case of positively charged particles (ZnO, Al₂O₃, Nd₂O₃, and Sm₂O₃ suspensions) and bromophenol blue for negatively charged particles (SiO₂ and Er₂O₃ suspensions; see the ζ potential curves in the Supporting Information, Figure SI-3). The dyes were added at a concentration of 10⁻⁴ and 2 × 10⁻⁵ mol·dm⁻³ in the case of bromophenol blue and patent blue V, respectively. The molar extinction coefficient of the two dyes as a function of the wavelength is given in Figure SI-4 in the Supporting Information. It does not depend on the pH in the range studied here (pH 6–10). The absence of interaction between the dye and the nanoparticles was checked by measurement of the absorbance of the dye for the same concentration in pure water and also in suspensions after centrifugation. Then, from the measured absorbance in a 1 mm optical path cell of the dye in pure water and in suspensions for which the baseline due to scattering is corrected, the real optical path can be deduced and is given in Table 2. All the figures containing the concentrations of the solvated electron presented hereafter were obtained by using this factor. We point out that this correction of the optical path is not needed in the case of Ludox as this solution is optically transparent.

γ Radiolysis. The γ radiolysis experiments were performed using the Gammacell 3000 Elan with a ¹³⁷Cs source. The dose rate 5.9 Gy/min (1 Gy = 1 J/kg) was determined using the Fricke dosimetry.^{42–44} To avoid the reaction of the electron with dioxygen, the solutions were carefully degassed by several cycles of argon/vacuum, bubbled with argon, and irradiated under an argon atmosphere.

Measurement of the Nitrite concentration Using the Shinn Method. In the Shinn method, the suspensions were centrifuged for 10 min at 14000 rpm after irradiation. A 250 μ L volume of supernatant was then mixed with 1 mL of HCl (15%) and 5 mL of sulfanilamide (0.2 wt %). The resulting solution was stirred for 5 min. It was then mixed with 1 mL of *N*-(1-naphthyl)ethylenediamine dihydrochloride (0.1 wt %) and stirred for 10 min. The absorbance of the pink rose dye formed was measured at 540 nm using a Shimadzu spectrophotometer. Calibration curves were performed in water and in the same suspensions as those which underwent

irradiation. In all cases, the molar extinction coefficient of the dye was found to be the same and equal to $51100 \pm 1200 \text{ dm}^3 \cdot \text{mol}^{-1} \cdot \text{cm}^{-1}$ at 540 nm, which is in good agreement with the value of $53200 \text{ dm}^3 \cdot \text{mol}^{-1} \cdot \text{cm}^{-1}$ found by Hayon.⁴⁵

RESULTS AND DISCUSSION

Picosecond Pulse Radiolysis. Figure 1a shows evidence that the picosecond transient spectrum directly after the energy

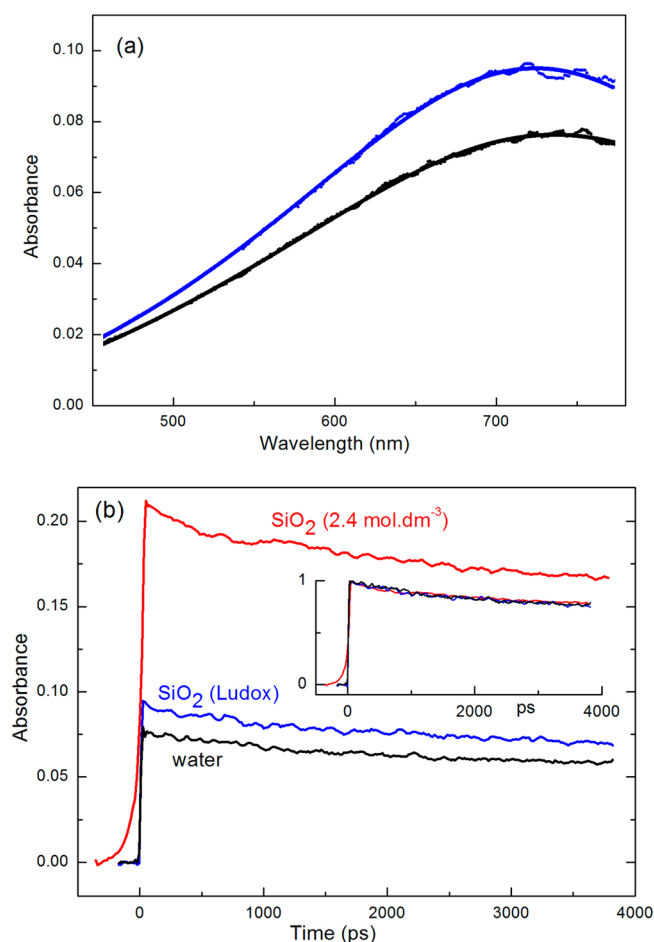


Figure 1. Picosecond radiolysis of pure water and silica suspensions in a cell of 5 mm optical path length: (a) transient absorption of the solvated electron after the 10 ps electron pulse in water (black) and in Ludox (blue); (b) evolution of the absorbance displayed at 720 nm in the 0–4 ns time scale range in water (black), Ludox (blue), and a $2.4 \text{ mol} \cdot \text{dm}^{-3}$ silica nanoparticle suspension (red). The three kinetics, normalized at their initial absorbance value, are shown in the inset, revealing that the three decays are the same.

absorption of the optically transparent Ludox solution (50% silica by weight) is the same as in pure water, both in shape and in spectral position. It is therefore attributed to the solvated electron. The corresponding kinetics traced at 720 nm is displayed in Figure 1b and compared to that of the highly scattering, concentrated silica nanoparticle suspension. The latter was recorded at 782 nm, and its amplitude scaled with the known extinction coefficients to 720 nm. The inset with the normalized kinetics proves that the decay of the solvated electron is identical within the measurement sensitivity in water, Ludox, and the concentrated silica nanoparticle suspension on the observed time scale to 4 ns, proving that the reactions of the electron within the spurs are identical in

these three systems. Assuming that the molar extinction coefficient of the electron is the same in these three samples, the increase in absorbance in the Ludox solution (blue curve in Figure 1b) is due to the increase in electron density as already shown in ref 28. Knowing the absorption amplitude (Figure 1b), the absorbed dose, and the density for water and Ludox, the ratio between the electron radiolytic yields of Ludox and water is calculated to be about 0.9, which is within the measurement sensitivities consistent with a previous experiment.²⁸ As Ludox is a 50 wt % silica sample, electrons are clearly transferred from silica into water under ionizing radiation. The increase in the silica nanoparticle suspension (red curve in Figure 1b) is attributed to the increase in electron density and also to the increased optical path of the probe light due to the scattering of the suspension (1.5 times higher for a 1 mm optical path cell; see Table 2). In both silica suspensions, the same electron kinetics as that in pure water is obtained.

Nanosecond Pulse Radiolysis. An example of a spectrum recorded in a nanoparticle suspension is presented in Figure 2

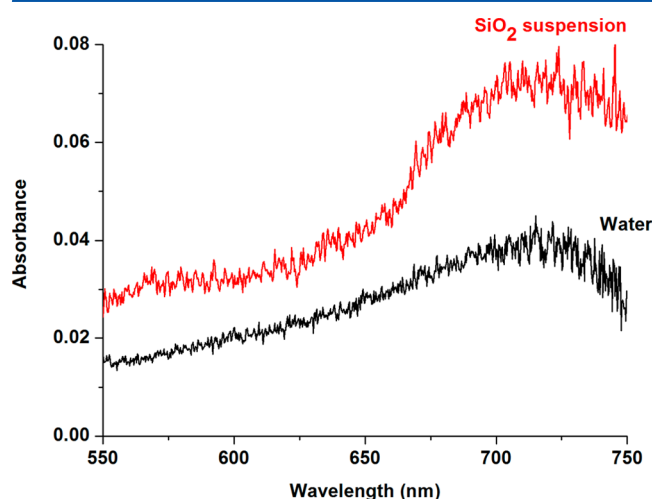


Figure 2. Spectrum of the solvated electron on the nanosecond time scale in water (black) and in a $0.6 \text{ mol} \cdot \text{dm}^{-3}$ SiO_2 suspension (red). The transient absorption is measured in a 1 mm cell after Ar bubbling. The signal measured under a N_2O atmosphere is subtracted.

for the SiO_2 system at 10 ns. The maximum is located at 715 nm as for pure water. This indicates that the solvated electron is detected and also justifies the use of the same molar extinction coefficient as that in water ($15800 \text{ dm}^3 \cdot \text{mol}^{-1} \cdot \text{cm}^{-1}$ at 633 nm). Spectra recorded in other suspensions lead to similar features and are thus not given here.

Using this value and all the characteristics of the different suspensions from Table 2 (calculation of the absorbed dose, correction of the optical path due to scattering, mass density), the different electron decay curves (Figures 3 and 4, for instance) enable us to calculate, from the value of the absorbance just after the pulse, the ratio between the electron radiolytic yields in suspensions and in water. The values are given in Table 3. The large uncertainties in the values are due to the light scattering of the solutions. The yields are in all cases greater than 1, which proves that electrons are always transferred from the oxide into water.

Some typical kinetics recorded on the microsecond scale in different suspensions and compared to that obtained in water are given in Figures 3 and 4. It is clear from Figure 3 that the solvated electron decay is the same for silica at pH 10.6 and 6.6

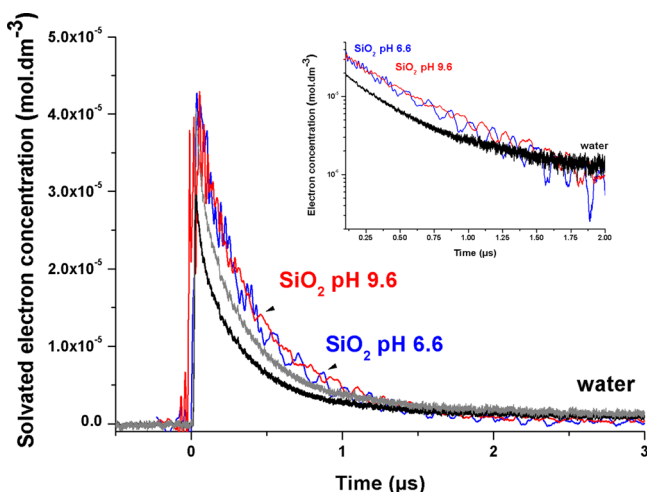


Figure 3. Decay of the solvated electron population recorded at 633 nm after radiolysis by a 10 ns electron pulse in a 1 mm optical path cell in water (black; normalized to the signal in silica in gray) and in 18 wt % SiO₂ suspensions at pH 6.6 (blue line) and pH 9.6 (red line). The decays are represented with a logarithmic scale in the inset. The decays follow a first-order law in the SiO₂ suspensions with a time constant $\tau = 430$ ns.

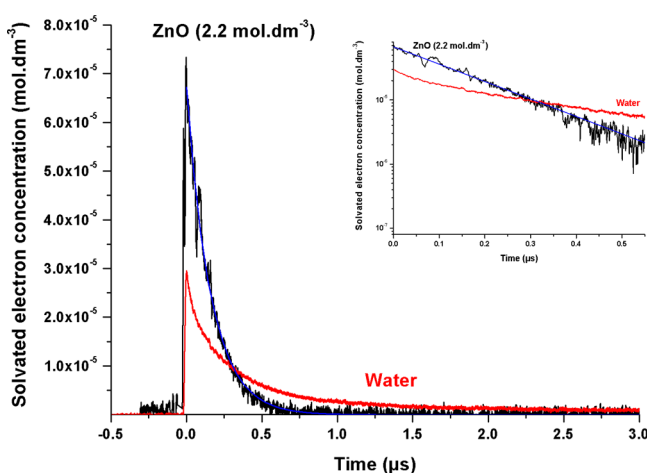


Figure 4. Solvated electron concentration decay recorded after 10 ns of electron pulse absorption at 633 nm in a 1 mm optical path cell in water (red) and in a 16 wt % ZnO suspension (black). The exponential decay of the solvated electron in the ZnO suspension is nicely fitted with the blue line characterized by a time constant $\tau = 160$ ns. The two decays are represented with a logarithmic scale in the inset.

and follows a first-order law. In these two cases, silica is negatively charged (Figure SI-3 in the Supporting Information). It may be pointed out that the solvated electron decay in silica can be attributed to the solvated electron reaction with the numerous $-\text{OH}$ groups which are present on the surface of the nanoparticles. It is worth noting that the solvated electron kinetics is slightly slower than in water (Figure 3), which can be linked to the high viscosity of the medium (more than 10 cP). Another example (decay of the solvated electron in a $0.6 \text{ mol}\cdot\text{dm}^{-3}$ Sm_2O_3 suspension) is given in Figure SI-5 in the Supporting Information.

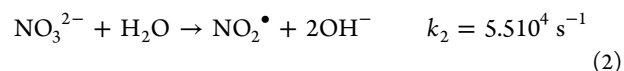
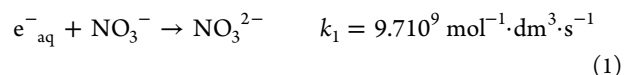
The solvated electron decay is also a first-order reaction in the case of the ZnO suspension (inset in Figure 4), and it is clearly largely accelerated in the ZnO suspension as compared

to water. This faster decay as compared to the silica case may be attributed to the reaction of the solvated electron with Zn^{2+} ions. It may be pointed out that the ZnO suspension is the only system in which a significant amount of ions can be found. The Zn^{2+} concentration was measured by atomic absorption spectroscopy to be $2 \times 10^{-5} \text{ mol}\cdot\text{dm}^{-3}$. This concentration is also consistent with the solubility of this oxide ($\text{p}K_s = 16.7$).

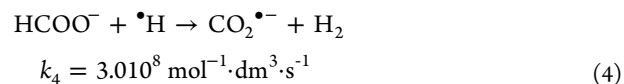
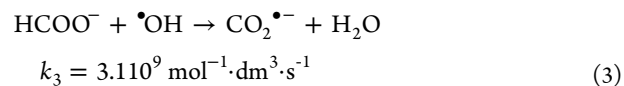
γ Radiolysis. Being sure by means of pulse radiolysis that the solvated electron is produced, another way to study it consists of scavenging it during steady-state radiolysis and studying the stable products after irradiation. One of the most widely used methods to determine its yield is to measure the nitrite yield in deoxygenated solutions containing nitrate ions as an electron scavenger together with $\cdot\text{OH}$ and $\cdot\text{H}$ scavengers.

Sodium nitrate (NaNO_3), which plays the role of an electron captor, was used at a concentration of $10^{-2} \text{ mol}\cdot\text{dm}^{-3}$. Higher concentrations of sodium nitrate change the nature of the solution because of interactions between sodium nitrate and nanoparticles and are not presented in this work.

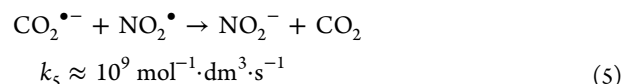
The solvated electron reacts with nitrate, leading to the formation of the dianion radical NO_3^{2-} (eq 1). This species will then lead to the formation of the $\text{NO}_2\cdot$ radical (eq 2).^{46–48} The main reactions are written below along with the rate constants taken from ref 49. It may be pointed out here that $k_1[\text{NO}_3^-] = 9.7 \times 10^7 \text{ s}^{-1}$, meaning that the characteristic time at which the electron is scavenged is roughly 10 ns. As revealed above by the time-resolved measurements (Figure 1b) which show that the decay kinetics are the same over the first 4 ns in water and in oxide suspensions, the yields obtained at 10 ns are representative of the ratio of the initial yields between the samples.



In the present study, the formate ion at a concentration of $10^{-2} \text{ mol}\cdot\text{dm}^{-3}$ was chosen to scavenge both $\cdot\text{OH}$ and $\cdot\text{H}$ radicals according to the following reactions:⁵⁰



The strongly reducing radical $\text{CO}_2^{\cdot-}$ then quickly converts the $\text{NO}_2\cdot$ radical into the nitrite ion:⁵¹



The nitrite radiolytic yield measured is then equal to the solvated electron radiolytic yield. It may be pointed out that another $\cdot\text{OH}$ scavenger (isopropanol) led to results similar to those presented below.

The obtained nitrites are then converted to a stable dye using the Shinn method.⁵² The nitrite concentration, and therefore the solvated electron concentration at 10 ns, is thus measured (Figure 5).

Table 3. Solvated Electron Radiolytic Yields, Normalized to That in Water, as a Function of the Oxide Suspension and of the Oxide Apparent Concentration^a

apparent concn (mol·dm ⁻³)	SiO ₂	ZnO	Al ₂ O ₃	Nd ₂ O ₃	Sm ₂ O ₃	Er ₂ O ₃	H ₂ O
Pulse Radiolysis Experiments							
2.2	1.3 ± 0.3	2.1 ± 0.6	1.4 ± 0.2				1
0.6		1.8 ± 0.6	1.3 ± 0.2		1.3 ± 0.2		
γ Irradiation Experiments							
2.2	1.04 ± 0.05		1.20 ± 0.04				1
0.6	1.05 ± 0.05	1.00 ± 0.04	1.01 ± 0.04	1.06 ± 0.05	1.20 ± 0.06	1.38 ± 0.06	

^aThe higher lines are the yields determined from pulse radiolysis experiments using the nanosecond ALIENOR linear electron accelerator. The solvated electron yield is deduced from the measured absorbance, assuming that, in all the studied suspensions, the molar extinction coefficient of the electron is 15800 dm³·mol⁻¹·cm⁻¹ at 633 nm. The lower lines are the nitrite radiolytic yields, and hence the solvated electron radiolytic yields, normalized to that obtained in water and determined using γ radiolysis. In our experimental conditions, $G(\text{NO}_2^-) = G(\text{e}_{\text{aq}}^-)$ (see the text). We find here $G(\text{e}_{\text{aq}}^-) = (3.22 \pm 0.15) \times 10^{-7}$ mol/J with 10^{-2} mol·dm⁻³ NaNO₃ and 10^{-2} mol·dm⁻³ HCOONa in water at 10 ns. This yield is in good agreement with the values obtained in refs 66 and 67.

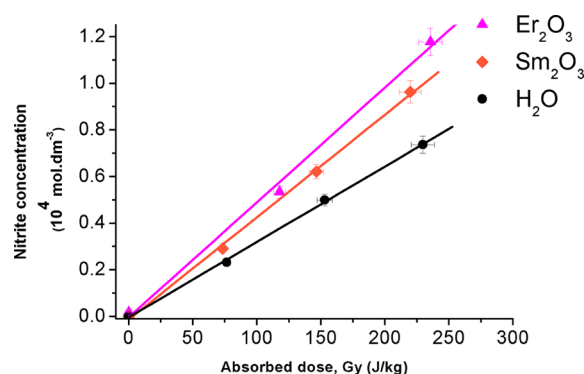


Figure 5. Nitrite concentration, and hence scavenged solvated electron concentration, obtained at $t = 10$ ns versus absorbed dose (FD ; see Table 2) for water (circles) and two oxides (Er_2O_3 , triangles; Sm_2O_3 , tilted squares) at an apparent concentration of $0.6 \text{ mol}\cdot\text{dm}^{-3}$ corresponding to oxide mass fractions of 0.2 and 0.185, respectively. The points are experimental data, and the lines are the corresponding linear fits.

For each suspension, the nitrite concentration, and hence the solvated electron concentration, can be plotted as a function of the absorbed dose (DF ; see Figure 5), where D is the dose received by water and determined by Fricke dosimetry and F is a correction factor³⁷ (Table 2). The nitrite radiolytic yield, and hence the solvated electron yield, can then be deduced from the slope of the lines (Figure 5) and from the density of each suspension. The different relative electron radiolytic yields as compared to water are then given in Table 3.

It may be pointed out that the radiolytic yields obtained in both experiments (by pulse or γ radiolysis) are consistent. In all cases, the electron radiolytic yield is slightly greater than or very similar to that obtained in pure water, indicating a very efficient electron transfer from the solid into the liquid phase. The results obtained in the case of silica are consistent with the work of Schatz et al.²⁸ For Sm_2O_3 and Er_2O_3 , the electron radiolytic yield is even slightly increased as compared to that in water (Table 3).

DISCUSSION

It appears clearly from the experiments and the deduced radiolytic yields summarized in Table 3 that whatever the band gap and the electron affinity of the oxide, electrons are transferred from the solid into water. This radiation-induced electron transfer can be compared to the photoinduced charge transfer which is of paramount importance in solar energy

conversion. In this latter case, it is well-known for the liquid phase that the redox structure is decoupled from the band structure.⁵³ For these semiconductor–liquid junctions, electrons can then be injected into redox couples (the $\text{H}_2\text{O}/\text{e}_{\text{aq}}^-$ redox couple here) and the continuity of the current is satisfied by ionic transport. In the present study, the same phenomena have to be considered (electron injection into the $\text{H}_2\text{O}/\text{e}_{\text{aq}}^-$ couple). Here we point out that a detailed theoretical treatment of interfacial electron transfer is difficult due to the lack of molecular models of the interface and because of the presence of inhomogeneities on the surfaces. Therefore, it will not be considered below.

Contrary to the conclusions of Ouerdane et al.,³⁰ who tried to generalize their simulations performed on porous silica, under ionizing radiation, electron injection from nanosized oxide into water always takes place, even if the bottom of the conduction band of the oxide is below the standard redox potential of the $\text{H}_2\text{O}/\text{e}_{\text{aq}}^-$ redox system (Scheme 1). This means that the electrons which are injected into water have not undergone thermalization before this process takes place: it is then a hot electron transfer. Indeed, if the electrons were thermalized, only the redox potentials that lie within the band gap of the oxide would have been available, which is not the case for all oxides, except alumina and silica (Scheme 1).

In the case of the high-loaded Al_2O_3 solutions ($2.2 \text{ mol}\cdot\text{dm}^{-3}$), and for Sm_2O_3 and Er_2O_3 ($0.6 \text{ mol}\cdot\text{dm}^{-3}$), the solvated electron yield is slightly enhanced as compared to that obtained in water (Table 3), which can seem surprising at first glance. An explanation is that energetic hot carriers may produce more electron–hole pairs thanks to impact ionization,⁵⁴ which is the inverse of an Auger recombination. This can be efficient only if the rate of this inverse Auger process is faster than the rate of carrier cooling. This effect can also account for the increasing electron yields with the oxide concentration in solution, as observed in Table 3 in the case of the ZnO and Al_2O_3 suspensions.

When γ radiation or an electron beam of a few megaelectronvolts interacts with the oxide, secondary electrons are emitted. Under ionizing radiation, the energy required to produce a charge-carrier pair can be found through the equation $2.73E_g + 0.55$ (eV), where E_g is the band gap energy.⁵⁵ For all oxides studied here, having a band gap ranging from 3.3 to 9.0 eV, and considering, for example, secondary electrons with a mean energy of about 100 eV, several electron–hole pairs (typically 4–10) may be formed in one particle. When the secondary electrons have more energy than

that required for producing a charge-carrier pair, then the thus generated electron and hole have excess energy and are called hot carriers. These hot carriers have an energy distribution. They can relax via electron–phonon interactions to get an energy near the band edge (bottom of the conduction band for an electron). Other relaxation pathways exist, such as exciton formation,^{56,57} trapping, etc. Concerning trapping, Tamaki et al. have, for instance, shown that electrons, whether they are hot or even trapped, created at any point in TiO₂ nanoparticles having a 20 nm diameter can move over the entire particle.⁵⁸ If hot electrons can be transferred at the interface before they relax to the bottom of the conduction band, then, whatever the electron affinity of the oxide, an electron transfer at the interface can be observed. Therefore, to account for our observations, we have to compare, in these nanoparticles, an estimate of the hot electron lifetime with the time required to go to the interface and to cross it. It may be pointed out here that no quantization effects in the semiconductors are expected, as the de Broglie wavelengths of the semiconductors are smaller than the size of the particles (20 nm). The transit time of an electron in the conduction band from the particle interior to the surface can be estimated as $\tau_{\text{transit}} = R^2/(D\pi^2)$,⁵⁹ with R the radius of the particle (10 nm) and D the diffusion coefficient of the electron (about 10^{-2} cm²·s⁻¹ in TiO₂, for instance⁵⁹). The transit time is then calculated to be on the order of 10 ps. Nevertheless, the migration of electrons must be faster when they have excess energy,⁵⁸ so this time should be smaller than 10 ps. The time required for the electron to cross the interface by tunneling also has to be taken into account. This tunneling time can be estimated and was found to be about 0.5 ps in the case of TiO₂.⁶⁰ Other times corresponding to cooling phenomena have to be compared: the intraband relaxation time and the interband electron–hole recombination. Even if these different times are not known for the various oxides used in the present study, comparable values can be found in the literature. Concerning the intraband relaxation, characteristic times of 4 ps have been reported in semiconductors.⁶¹ Lastly, the interband electron–hole recombination was, for instance, estimated to be about 100 ps in the case of TiO₂ having a carrier density of 2×10^{19} cm⁻³ and 100 ns for a carrier density of 10^{17} cm⁻³.⁶⁰ In the present study, a carrier density of 10^{18} cm⁻³ can be estimated. Therefore, it is possible, in these nanosized systems, that the rate of electron generation, transport, and transfer to the interface is faster than the cooling rate. Moreover, as pointed out above, hot carriers may produce more electron–hole pairs thanks to impact ionization. It may be pointed out that the efficiency of cooling phenomena can differ from one system to another, leading to the discrepancies in the measured radiolytic yields (Table 3). Lastly, electrons which have not undergone relaxation can be injected into water.

All of these estimates are then consistent with the fact that the same spectrum as that in water is recorded in Ludox (Figure 1a) using 10 ps electron pulses. Therefore, no distinction can be made between electrons arising from the solid and electrons produced directly in water. Only femto-second electron pulses could help differentiate both contributions in these nanometric oxide/water suspensions.

Nevertheless, electrons could also cross the interface in the opposite direction, going from water into the oxide conduction band. This is clearly not observed in the first nanoseconds of the experiments (Figure 1b). One explanation is that the oxide volume fraction is smaller than that of water, making this

electron transfer from water into the solid less probable than the electron transfer from the oxide into water, as already observed by Schatz et al.²⁸ Another explanation lies in the fast solvation of electrons in water (1 ps), which makes the electron transfer from water into the solid by tunneling less probable. This fast solvation leads to an irreversible electron transfer at the oxide/water interface. This irreversibility was attributed⁶² to the strong electronic–vibrational coupling in water, i.e., to the fact that relaxation is faster in the liquid than in the solid. The picosecond pulse radiolysis experiments evidence that the electron decay is the same within the first nanoseconds (Figure 1b) in water and in the oxide suspensions, as the reactions within the spurs are not modified in water and in the suspensions. This means that when the viscosity effect is not important (short time, short distance as for spur reactions), we have almost the same distribution of holes and solvated electrons, giving the same decays (Figure 1). Nevertheless, it then becomes very different on the nanosecond to microsecond time scale, once the electrons diffuse in solution. The decay of the solvated electrons in SiO₂ suspensions is indeed slower than in pure water. In fact, when the viscosity is high, the decay reactions of the solvated electrons at the microsecond time range cannot be due to those of recombination reactions but are mainly due to reactions with species at high concentration giving a first-order reaction (–OH groups at the interface). For the suspensions containing reactive metal cations (such as Zn²⁺), the decay of the solvated electron is faster than in pure water, even if the viscosity of the solution is higher. Therefore, we have to consider that the reaction rate of the solvated electrons with –OH groups at the interface is slow compared to that with reactive metal cations such as Zn²⁺. It may be pointed out that a faster electron decay has already been reported in Ludox as compared to water in the microsecond time scale range.²⁸ The trends reported here are less clear. The slower kinetics in the case of the silica and Sm₂O₃ suspensions, for instance (Figure 3 and Figure SI-5 in the Supporting Information, respectively), may be attributed to the high viscosity of the medium.

Lastly, it may be pointed out that hot holes generally cool faster than hot electrons. That is why the question of hot carriers is generally restricted to electrons.⁶³ The question raised here is then to determine the fate of the oxidation equivalents created in the particles. Previous studies performed in silica particles⁶⁴ evidence that the holes do not migrate from the particles to water. Other studies in TiO₂,⁶⁵ for instance, prove that holes can oxidize water. The fate of the holes is then not clear and should be the purpose of another study.

CONCLUSION

The solvated electron formation in oxide/water nanosuspensions of SiO₂, ZnO, Al₂O₃, Nd₂O₃, Sm₂O₃, and Er₂O₃ was studied after pulse and γ radiolysis. In all cases, electrons are transferred from the particles into water. This electron transfer can be very efficient as hot carriers may produce more electron–hole pairs thanks to impact ionization. Irradiation leads to the formation of hot electrons that can irreversibly cross the interface, as the rate of electron production and transfer to the interface is faster than the cooling rate in these nanometric oxides. Using the picosecond time scale, it was possible to show that the solvated electron spectrum is the same in these suspensions as in water. It would then be interesting to work with femtosecond electron pulses to distinguish between the electrons directly produced in water

and those which arise from the energy absorption of the solid. Moreover, picosecond and nanosecond radiolyses evidence that, if the solvated electron decay is the same as in water on the picosecond to nanosecond time scale (the reactions in the spurs being not affected by the oxide particles), it is completely different in the nanosecond to microsecond time range (due to the diffusion of the solvated electrons). In this latter case, the changes can be attributed to the modification of the viscosity of the medium, as well as to a reaction with impurities present and/or to reactions with the numerous $-OH$ groups which are present on the surface of the nanoparticles. Lastly, it would be interesting to study the fate of the oxidizing equivalents of the electrons (holes) created in these systems.

Ionizing radiation then induces an original reactivity in these nanosized systems: even small band gap oxides can generate an electron transfer at the oxide/water interface.

■ ASSOCIATED CONTENT

■ Supporting Information

Choice of optimal sonication conditions, CRYO-TEM photo of a suspension, ζ potential curves of the different suspensions, molar extinction coefficient curves of bromophenol blue and patent blue V, decay of the solvated electron concentration in water and in a $0.6 \text{ mol} \cdot \text{dm}^{-3} \text{ Sm}_2\text{O}_3$ suspension on the nanosecond to microsecond time scale, and viscosity of the suspensions. This material is available free of charge via the Internet at <http://pubs.acs.org>.

■ AUTHOR INFORMATION

Corresponding Author

*Phone: +33 1 69 08 15 58. Fax: +33 1 69 08 34 66. E-mail: sophie.le-caer@cea.fr.

Notes

The authors declare no competing financial interest.

■ ACKNOWLEDGMENTS

Triangle de la physique and Commissariat à l'énergie atomique et aux énergies alternatives are gratefully acknowledged for financial support. Dr. Alexandre Dazzi is acknowledged for preliminary AFM experiments. We thank Pr. Cécile Sicard for her help with the dynamic light scattering experiments and Dr. Dominique Gosset for help with the powder X-ray diffraction experiments. Dr. Jean Philippe Renault is gratefully acknowledged for fruitful discussion and Dr. Gérard Baldacchino for his help in the nanosecond pulse radiolysis experiments.

■ REFERENCES

- (1) Sun, W.; Gao, R.; Jiao, K. Electrochemistry and Electrocatalysis of Hemoglobin in Nafion/Nano- CaCO_3 Film on a New Ionic Liquid BPPF₆ Modified Carbon Paste Electrode. *J. Phys. Chem. B* **2007**, *111*, 4560–4567.
- (2) Schmuki, P.; Virtanen, S. *Electrochemistry at the Nanoscale*; Springer: New York, 2009.
- (3) Wang, H.; Bai, Y.; Wu, Q.; Zhou, W.; Zhang, H.; Li, J.; Guo, L. Rutile TiO_2 Nano-Branched Arrays on FTO for Dye-Sensitized Solar Cells. *Phys. Chem. Chem. Phys.* **2011**, *13*, 7008–7013.
- (4) Hong, Y. C.; Sun, K. Q.; Zhang, G. R.; Zhong, R. Y.; Xu, B. Q. Fully Dispersed Pt Entities on Nano-Au Dramatically Enhance the Activity of Gold for Chemoselective Hydrogenation Catalysis. *Chem. Commun.* **2011**, *47*, 1300–1302.
- (5) Zhang, Y.; Cui, X.; Shi, F.; Deng, Y. Nano-Gold Catalysis in Fine Chemical Synthesis. *Chem. Rev.* **2012**, *112*, 2467–2505.
- (6) Shi, F.; Tse, M. K.; Pohl, M. M.; Bruckner, A.; Zhang, S.; Beller, M. Tuning Catalytic Activity between Homogeneous and Heterogeneous Catalysis: Improved Activity and Selectivity of Free Nano- Fe_2O_3 in Selective Oxidations. *Angew. Chem., Int. Ed.* **2007**, *46*, 8866–8868.
- (7) Vadivel Murugan, A.; Muraliganth, T.; Ferreira, P. J.; Manthiram, A. Dimensionally Modulated, Single-Crystalline LiMPO_4 (M= Mn, Fe, Co, and Ni) with Nano-Thumblike Shapes for High-Power Energy Storage. *Inorg. Chem.* **2009**, *48*, 946–952.
- (8) Jo, C.; An, S.; Kim, Y.; Shim, J.; Yoon, S.; Lee, J. Nano-Graphite Functionalized Mesocellular Carbon Foam with Enhanced Intra-Penetrating Electrical Percolation Networks for High Performance Electrochemical Energy Storage Electrode Materials. *Phys. Chem. Chem. Phys.* **2012**, *14*, 5695–5704.
- (9) Wang, H.; Dai, H. Strongly Coupled Inorganic-Nano-Carbon Hybrid Materials for Energy Storage. *Chem. Soc. Rev.* **2013**, *42*, 3088–3113.
- (10) Ashwell, G. J.; Wierzchowiec, P.; Bartlett, C. J.; Buckle, P. D. Molecular Electronics: Connection across Nano-Sized Electrode Gaps. *Chem. Commun.* **2007**, 1254–1256.
- (11) Lyshevski, S. E. *Nano and Molecular Electronics Handbook*; Taylor & Francis: Boca Raton, FL, 2007.
- (12) Iniewski, K. *Nanoelectronics: Nanowires, Molecular Electronics, and Nanodevices*; McGraw-Hill: New York, 2011.
- (13) Paulus, G. L.; Ham, M. H.; Strano, M. S. Anomalous Thickness-Dependence of Photocurrent Explained for State-of-the-Art Planar Nano-Heterojunction Organic Solar Cells. *Nanotechnology* **2012**, *23*, 095402.
- (14) Lin, G. R.; Meng, F. S.; Pai, Y. H.; Lin, Y. H. Enhanced Conversion Efficiency and Surface Hydrophobicity of Nano-Roughened Teflon-Like Film Coated Poly-Crystalline Si Solar Cells. *Phys. Chem. Chem. Phys.* **2012**, *14*, 3968–3973.
- (15) Pivac, B.; Dubcek, P.; Capan, I.; Zulim, I.; Betti, T.; Zorc, H.; Bernstorff, S. Nano Si Superlattices for the Next Generation Solar Cells. *J. Nanosci. Nanotechnol.* **2009**, *9*, 3853–3857.
- (16) Eom, S. H.; Senthilarasu, S.; Yoon, S. C.; Lee, J.; Lee, S. H. Nano-Scale ZnO Buffer Layer for Inkjet-Printed Polymer Solar Cells. *J. Nanosci. Nanotechnol.* **2008**, *8*, 5113–5117.
- (17) Ho, S. Y.; Su, C.; Cheng, C. C.; Kathirvel, S.; Li, C. Y.; Li, W. R. Preparation, Characterization, and Application of Titanium Nano-Tube Array in Dye-Sensitized Solar Cells. *Nanoscale Res. Lett.* **2012**, *7*, 147.
- (18) Hart, E. J.; Boag, J. W. Absorption Spectrum of the Hydrated Electron in Water and in Aqueous Solutions. *J. Am. Chem. Soc.* **1962**, *84*, 4090–4095.
- (19) Bronskill, M. J.; Taylor, W. B.; Wolff, R. K.; Hunt, J. W. Design and Performance of a Pulse Radiolysis System Capable of Picosecond Time Resolution. *Rev. Sci. Instrum.* **1970**, *41*, 333–340.
- (20) Jonah, C. D.; Matheson, M. S.; Miller, J. R.; Hart, E. J. Yield and Decay of the Hydrated Electron from 100 ps to 3 ns. *J. Phys. Chem.* **1976**, *80*, 1267–1270.
- (21) Bartels, D. M.; Cook, A. R.; Mudaliar, M.; Jonah, C. D. Spur Decay of the Solvated Electron in Picosecond Radiolysis Measured with Time-Correlated Absorption Spectroscopy. *J. Phys. Chem. A* **2000**, *104*, 1686–1691.
- (22) Wishart, J. F.; Cook, A. R.; Miller, J. R. The LEAF Picosecond Pulse Radiolysis Facility at Brookhaven National Laboratory. *Rev. Sci. Instrum.* **2004**, *75*, 4359–4366.
- (23) Muroya, Y.; Lin, M.; Wu, G.; Iijima, H.; Yoshii, K.; Ueda, T.; Kudo, H.; Katsumura, Y. A Re-Evaluation of the Initial Yield of the Hydrated Electron in the Picosecond Time Range. *Radiat. Phys. Chem.* **2005**, *72*, 169–172.
- (24) Lin, M.; Kumagai, Y.; Lampre, I.; Coudert, F. X.; Muroya, Y.; Boutin, A.; Mostafavi, M.; Katsumura, Y. Temperature Effect on the Absorption Spectrum of the Hydrated Electron Paired with a Lithium Cation in Deuterated Water. *J. Phys. Chem. A* **2007**, *111*, 3548–3553.
- (25) Dey, G. R.; El Omar, A. K.; Jacob, J. A.; Mostafavi, M.; Belloni, J. Mechanism of Trivalent Gold Reduction and Reactivity of Transient Divalent and Monovalent Gold Ions Studied by Gamma and Pulse Radiolysis. *J. Phys. Chem. A* **2011**, *115*, 383–391.
- (26) Schmidhammer, U.; Pernot, P.; De Waele, V.; Jeunesse, P.; Demarque, A.; Murata, S.; Mostafavi, M. Distance Dependence of the

Reaction Rate for the Reduction of Metal Cations by Solvated Electrons: a Picosecond Pulse Radiolysis Study. *J. Phys. Chem. A* **2010**, *114*, 12042–12051.

(27) Brown, G. E., Jr.; Henrich, V. E.; Casey, W. H.; Clark, D. L.; Eggleston, C.; Felmy, A.; Goodman, D. W.; Grätzel, M.; Maciel, G.; McCarthy, M. L.; Neelson, K. H.; Sverjensky, D. A.; Toney, M. F.; Zachara, J. M. Metal Oxide Surfaces and Their Interactions with Aqueous Solutions and Microbial Organisms. *Chem. Rev.* **1999**, *99*, 77–174.

(28) Schatz, T.; Cook, A. R.; Meisel, D. Charge Carrier across the Silica/Nanoparticle Water Interface. *J. Phys. Chem. B* **1998**, *102*, 7225–7230.

(29) Musat, R. M.; Cook, A. R.; Renault, J. P.; Crowell, R. A. Nanosecond Pulse Radiolysis of Nanoconfined Water. *J. Phys. Chem. C* **2012**, *116*, 13104–13110.

(30) Ouerdane, H.; Gervais, B.; Zhou, H.; Beuve, M.; Ph, R. J. Radiolysis of Water Confined in Porous Silica: A Simulation Study of the Physicochemical Yields. *J. Phys. Chem. C* **2010**, *114*, 12667–12674.

(31) Kanaya, K.; Ono, S.; Ishigaki, F. Secondary Electron Emission from Insulators. *J. Phys. D: Appl. Phys.* **1978**, *11*, 2425–2437.

(32) Seiler, H. Secondary Electron Emission in the Scanning Electron Microscope. *J. Appl. Phys.* **1983**, *54*, R1–R18.

(33) Gbur, T.; Cuba, V.; Mucka, V.; Nikl, M.; Knizek, K.; Pospisil, M.; Jakubec, I. Photochemical Preparation of ZnO Nanoparticles. *J. Nanopart. Res.* **2011**, *13*, 4529–4537.

(34) Mandzy, N.; Grulke, E.; Druffel, T. Breakage of TiO₂ Agglomerates in Electrostatically Stabilized Aqueous Dispersions. *Powder Technol.* **2005**, *160*, 121–126.

(35) Qi, J.; Ye, Y. Y.; Wu, J.; Wang, H. T.; Li, F. T. Dispersion and Stability of Titanium Dioxide Nanoparticles in Aqueous Suspension: Effects of Ultrasonication and Concentration. *Water Sci. Technol.* **2013**, *67*, 147–151.

(36) Taurozzi, J. S.; Hackley, V. A.; Wiesner, M. R. Preparation of Nanoparticle Dispersions from Powdered Material Using Ultrasonic Disruption. *Natl. Inst. Stand. Technol. Spec. Publ.* **2000-2** **2012**, 1–14.

(37) Pucheault, J.; Ferradini, C.; Julien, R.; Deysine, A.; Gilles, L.; Moreau, M. Radiolysis of Concentrated Solutions. I. Pulse and Gamma Radiolysis Studies of Direct and Indirect Effects in Lithium Chloride Solutions. *J. Phys. Chem.* **1979**, *83*, 330–336.

(38) Belloni, J.; Monard, H.; Gobert, F.; Larbre, J.-P.; Demarque, A.; De Waele, V.; Lampre, I.; Marignier, J.-L.; Mostafavi, M.; Bourdon, J. C.; Bernard, M.; Borie, H.; Garvey, T.; Jacquemard, B.; Leblond, B.; Lepercq, P.; Omeich, M.; Roch, M.; Rodier, J.; Roux, R. ELYSE-A Picosecond Electron Accelerator for Pulse Radiolysis Research. *Nucl. Instrum. Methods Phys. Res., A* **2005**, *539*, 527–539.

(39) Mialocq, J. C.; Hickel, B.; Baldacchino, G.; Juillard, M. The Radiolysis project of CEA. *J. Chim. Phys.* **1999**, *96*, 35–43.

(40) Jou, F.-Y.; Freeman, G. R. Shapes of Optical Spectra of Solvated Electrons. Effect of Pressure. *J. Phys. Chem.* **1977**, *81*, 909–915.

(41) Butler, W. L. Absorption of Light by Turbid Materials. *J. Opt. Soc. Am.* **1962**, *52*, 292–299.

(42) Sutton, H. C. A Calibration of the Fricke Chemical Dosimeter. *Phys. Med. Biol.* **1956**, *1*, 153–160.

(43) Himitt, M.; Itoh, T.; Endo, S.; Fujikawa, K.; Hoshi, M. Dosimetry of Mixed Neutron and Gamma Radiation with Paired Fricke Solutions in Light and Heavy Water. *J. Radiat. Res.* **1996**, *37*, 97–106.

(44) Sanguanmith, S.; Muroya, Y.; Tippayamontri, T.; Meesungnoen, J.; Lin, M.; Katsumura, Y.; Jay-Gerin, J. P. Temperature Dependence of the Fricke Dosimeter and Spur Expansion Time in the Low-LET High-Temperature Radiolysis of Water up to 350°C: a Monte-Carlo Simulation Study. *Phys. Chem. Chem. Phys.* **2011**, *13*, 10690–10698.

(45) Hayon, E. Solute Scavenging Effects in Regions of High Radical Concentration Produced in Radiation Chemistry. *Trans. Faraday Soc.* **1965**, *61*, 723–733.

(46) Daniels, M.; Wigg, E. E. Radiation Chemistry of the Aqueous Nitrate System. I. Gamma-Radiolysis of Dilute Solutions. *J. Phys. Chem.* **1967**, *71*, 1024–1033.

(47) Faraggi, M.; Zehavi, D.; Anbar, M. Radiolysis of Aqueous Nitrate Solutions. *Trans. Faraday Soc.* **1971**, *67*, 701–710.

(48) Cook, A. R.; Dimitrijevic, N.; Dreyfus, B. W.; Meisel, D.; Curtiss, L. A.; Camaioni, D. M. Reducing Radicals in Nitrate Solutions. The NO₃²⁻ System Revisited. *J. Phys. Chem. A* **2001**, *105*, 3658–3666.

(49) Buxton, G. V.; Greenstock, C. L.; Helman, W. P.; Ross, A. B. Critical Review of Rate Constants for Reactions of Hydrated Electrons, Hydrogen Atoms and Hydroxyl Radicals (OH/O⁻) in Aqueous Solution. *J. Phys. Chem. Ref. Data* **1988**, *17*, 513–886.

(50) Ponomarev, A. V.; Bludenko, A. V.; Makarov, I. E. Effect of Formate on the Radiolytic Degradation of Nitrate in Deaerated Aqueous Solutions. *Mendeleev Commun.* **2002**, *12*, 92–94.

(51) Elliott, A. J.; Simons, A. S. *Reactions of NO₂ and Nitrite Ion with Organic Radicals*; NRC Research: Plattsburgh, NY, 1984; Vol. 62.

(52) Shinn, M. B. Colorimetric Method for Determination of Nitrate. *Ind. Eng. Chem., Anal. Ed.* **1941**, *13*, 33–35.

(53) Williams, F.; Nozik, A. J. Solid-State Perspectives of the Photoelectrochemistry of Semiconductor-Electrolyte Junctions. *Nature* **1984**, *312*, 21–27.

(54) Kolodinski, S.; Werner, J. H.; Wittchen, T.; Queisser, H. J. Quantum Efficiencies Exceeding Unity due to Impact Ionization in Silicon Solar Cells. *Appl. Phys. Lett.* **1993**, *63*, 2405–2407.

(55) Alig, R. C.; Bloom, S. Electron-Hole-Pair Creation Energies in Semiconductors. *Phys. Rev. Lett.* **1975**, *35*, 1522–1525.

(56) Le Caër, S.; Rotureau, P.; Brunet, F.; Charpentier, T.; Blain, G.; Renault, J. P.; Mialocq, J. C. Radiolysis of Confined Water: Hydrogen Production at a High Dose Rate. *ChemPhysChem* **2005**, *6*, 2585–2596.

(57) Brodie-Linder, N.; Le Caër, S.; Alam, M. S.; Renault, J. P.; Alba-Simionesco, C. H₂ Formation by Electron Irradiation of SBA-15 Materials and the Effect of Cu^{II} Grafting. *Phys. Chem. Chem. Phys.* **2010**, *12*, 14188–14195.

(58) Tamaki, Y.; Hara, K.; Katoh, R.; Tachiya, M.; Furube, A. Femtosecond Visible-to-IR Spectroscopy of TiO₂ Nanocrystalline Films: Elucidation of the Electron Mobility before Deep Trapping. *J. Phys. Chem. C* **2009**, *113*, 11741–11746.

(59) Grätzel, M.; Frank, A. J. Interfacial Electron-Transfer Reactions In Colloidal Semiconductor Dispersions. Kinetic Analysis. *J. Phys. Chem.* **1982**, *86*, 2964–2967.

(60) Williams, F.; Nozik, A. J. Irreversibilities in the Mechanism of Photoelectrolysis. *Nature* **1978**, *271*, 137–139.

(61) Shank, C. V.; Fork, R. L.; Leheny, R. F.; Shah, J. Dynamics of Photoexcited GaAs Band-Edge Absorption with Subpicosecond Resolution. *Phys. Rev. Lett.* **1979**, *42*, 112–115.

(62) Boudreaux, D. S.; Williams, F.; Nozik, A. J. Hot Carrier Injection at Semiconductor-Electrolyte Junctions. *J. Appl. Phys.* **1980**, *51*, 2158–2163.

(63) Nozik, A.; Memming, R. Physical Chemistry of Semiconductor-Liquid Interfaces. *J. Phys. Chem.* **1996**, *100*, 13061–13078.

(64) Dimitrijevic, N. M.; Henglein, A.; Meisel, D. Charge Separation across the Silica Nanoparticle/Water Interface. *J. Phys. Chem. B* **1999**, *103*, 7073–7076.

(65) Cowan, A. J.; Tang, J.; Leng, W.; Durrant, J. R.; Klug, D. R. Water Splitting by Nanocrystalline TiO₂ in a Complete Photoelectrochemical Cell Exhibits Efficiencies Limited by Charge Recombination. *J. Phys. Chem. C* **2010**, *114*, 4208–4214.

(66) Pimblott, S. M.; LaVerne, J. A. Cooperative Effects of Scavengers on the Scavenged Yield of the Hydrated Electron. *J. Phys. Chem.* **1992**, *96*, 8904–8909.

(67) Draganic, Z. D.; Draganic, I. G. Formation of Primary Yields of Hydroxyl Radical and Hydrated Electron in the Gamma-Radiolysis of Water. *J. Phys. Chem.* **1973**, *77*, 765–772.